ChemElectroChem

Research Article
doi.org/10.1002/celc.202400656

Chemistry Europe
European Chemical Societies Publishing

www.chemelectrochem.org

# Understanding the Role of Varying $Ti_3C_2T_x$ MXene in Ni/$Ti_3C_2T_x$ for the Oxygen Evolution Reaction

Gabriel Schröder,[a] Saeed Sajjadi,[a, b] Bastian Schmiedecke,[a] Aline Alencar Emerenciano,[a] Thorsten Schultz,[c, d] Norbert Koch,[c, d] Merve Buldu-Akturk,*[a] and Michelle P. Browne*[a]

The current state-of-the-art catalysts for the oxygen evolution reaction (OER) in an anion exchange membrane (AEM) electrolyser are not efficient enough to surpass green $H_2$ produced by other electrolyser technologies, such as Proton Exchange Membrane (PEM) electrolysers. One reason for this is due to the AEM catalysts not being active enough and lacking long-term stability. In this work, we combine Ni based material with $Ti_3C_2T_x$ MXene at different loadings (1, 5 and 10%) to understand the effect of the MXene on the OER activity and stability. Our results show that the amount of MXene not only affects the OER performance, but the materials surface is also altered. Interestingly, the $Ti_3C_2T_x$ is still present in the bulk for all composites but the surface of the composites contains different amounts of oxidized $Ti_3C_2T_x$ i.e. $TiO_2$. The optimum material in this study for the OER is the $NiO_x$/1%$Ti_3C_2T_x$ which can be rationalized by the lower Ti/Ni ratio in the starting materials hence producing less overall surface $TiO_2$ during OER. Additionally, when the pure $NiO_x$ and the 1% Ni-$Ti_3C_2T_x$ are compared by operando Raman spectroscopy, the $NiO_x$/1%$Ti_3C_2T_x$ exhibits β-NiOOH at lower overpotentials, which is known to be present for efficient OER on Ni materials.

## 1. Introduction

Since the beginning of the industrial revolution, the foundation of the global energy infrastructure has been largely based on fossil fuels. However, this dependence has also resulted in adverse consequences, including the emission of greenhouse gases and the contamination of the environment, which have become the driving force behind the pursuit of cleaner energy alternatives. The social and political efforts to transition towards affordable green electricity are multifaceted, including solar, geothermal, hydropower, biomass and wind, but must aim to minimize emissions as much as possible and ensure economic viability. To potentially meet these requirements, green hydrogen ($H_2$) repeatedly emerges in this context as a forward-looking energy carrier with broad application potential as a clean and renewable fuel.[1,2] The development of suitable water splitting techniques and associated materials is therefore conceivably suitable for utilizing the advantages of hydrogen since it is regarded as a friendly and promising process for converting energy from renewable resources into chemically bound energy by means of an electrocatalytic route.[3,4]

Water splitting can be divided into two partial reactions: the hydrogen evolution reaction (HER) at the cathode, and the oxygen evolution reaction (OER) at the anode.[5,6] Research focuses primarily on these two half-reactions, as they are essential for optimizing the overall efficiency of water splitting.[7] The OER is a multi-step process involving both the active catalyst surface and the intermediate of the overall reaction, resulting in a greater energy input compared to the HER. Due to this and the slow kinetics of the adsorption processes, the OER is the limiting factor in the overall energy balance of water splitting, which results in an increased overpotential.[8] This fact makes the research and development of more efficient OER catalysts inevitable in order to pave the way for better performing water splitting systems and is of great interest to build a more sustainable energy landscape worldwide.

Many electrocatalysts have been developed based on the consideration to lower the activation energy that dictates the kinetics of the reaction and is needed to drive the water splitting reaction itself to improve the overall efficiency of the OER.[9–11] These include metals and oxides from the platinum metal group, such as iridium (Ir) and ruthenium (Ru) based materials, which have long been known for their OER activity.[12–14] Although these catalysts remain among the most efficient catalysts in both the acidic and basic media and are useful for benchmarking or as cocatalysts, their widespread use

[a] G. Schröder, S. Sajjadi, B. Schmiedecke, A. A. Emerenciano, M. Buldu-Akturk, M. P. Browne
Helmholtz Young Investigator Group Electrocatalysis: Synthesis to Devices, Helmholtz-Zentrum Berlin für Materialien und Energie, 14109 Berlin, Germany
E-mail: merve.aktuerk@helmholtz-berlin.de
michelle.browne@helmholtz-berlin.de

[b] S. Sajjadi
Centre for Functional and Surface Functionalized Glass, Alexander Dubček University of Trenčín, Trenčín, 911 50, Slovakia

[c] T. Schultz, N. Koch
Helmholtz-Zentrum Berlin für Materialien und Energie GmbH, 14109, Berlin, Germany

[d] T. Schultz, N. Koch
Institut für Physik & IRIS Adlershof, Humboldt-Universität zu Berlin, Berlin, Germany

Supporting information for this article is available on the WWW under https://doi.org/10.1002/celc.202400656

is bound by several obstacles, such as low long-term stability in alkaline environment, high costs and scarce availability.[15,16]

Among various non-noble-transition-metal-based water splitting catalysts, transition metal oxides (TMOs) in particular have emerged as promising candidates for OER because a large-scale preparation is more feasible than the synthesis of other counterparts of OER catalysts.[7,15,17] Among those, Ni-based materials have been extensively studied over the years and are known for their enhanced OER activity. For $Ni(OH)_2$, a phase conversion occurs by electrochemical cycling in alkaline media, dehydrating the lattice layers and altering the layer spacing, which leads to increased electrochemical activity for the OER.[18,19] It has been shown that many Ni-based catalysts act as pre-catalysts, undergoing dynamic reconstruction under oxidative conditions, which result in the formation of an oxyhydroxide layer as active surface.[20–23] Several factors can influence the activity of the Ni catalysts, including irreversible changes like morphological and structural transformations, as well as reversible processes such as oxygen vacancy dynamics, phase transformations, surface atom dissolution/redeposition and intermediate adsorption/desorption.[21,24] A major drawback of TMOs is their inferior electrical conductivity, which has driven research into solutions involving carbon-based additives as support materials.

Among these studies are those investigating the use of MXenes as a 2D auxiliary material, as they can help to improve the OER by increasing the active surface area and reducing the amount of catalyst needed to hold the same degree of activity as without the use of MXenes.[25–30] MXenes are a class of two-dimensional transition metal carbides, nitrides or carbonitrides that was first reported in 2011.[31] With a general formula of $M_{n+1}X_nT_x$ ($n = 1–3$), where $n+1$ layers of early transition metals (M) such as Ti, V, or Nb cover n layers carbon or nitrogen (X), with surface terminations ($T_x$) such as $O^-$, $OH^-$, $F^-$ or $Cl^-$ that vary depending on the synthesis conditions.[31,32] Typically, $Ti_3C_2T_x$ MXenes are prepared by selectively etching aluminum (A) from the MAX phase ($Ti_3AlC_2$) by preserving the 2D structure of the $Ti_3AlC_2$.[33,31,34] Due to the fact that the surface terminations can be tuned by the synthetic procedure during the exfoliation, a great potential arises as beneficial interactions with the catalysts sides during the OER.[35] For instance chemical bonds between MXene and metal oxide (–O/–OH groups) can influence the conductivity and catalytic activity of the composite by preventing agglomeration with the effect of a uniform catalytic distribution on the surface of the electrode.[36] Besides this advantage, other characteristics appear that make MXenes interesting from a research perspective, including a high electrical conductivity that can reach up to 20,000 $S\,cm^{-1}$ ($Ti_3C_2T_x$).[37,38] Beyond that, MXenes are distinguished from other 2D-nanomaterials by their customizable compositions, which render them highly versatile for applications in OER catalysis.[39]

$Ti_3C_2T_x$, one of the most studied MXenes, is a promising supporting material for OER for different metal oxide-based systems.[40] For example, Lu *et al.* investigated the influence of $Ti_3C_2T_x$ content on the OER activity of $Co_3O_4/Ti_3C_2T_x$ hybrids by synthesizing materials with varying $Ti_3C_2T_x$ ratios using a solvothermal method. The $Co_3O_4/Ti_3C_2T_x$ hybrid containing 10% MXene showed an overpotential of 300 mV at 10 $mA\,cm^{-2}$ which exhibited enhanced OER performance compared to hybrids with higher MXene concentrations.[41] In another study, Jia *et al.* reported that the MXene structure provided additional mass transport pathways for OER. The MXene-$Ni_{0.075}Mn_{0.925}O_2$ electrodeposited on a carbon cloth (CC) displayed an overpotential of ~410 mV at a current density of 50 $mA\,cm^{-2}$, outperforming the $Ni_{0.075}Mn_{0.925}O_2$/CC catalyst by 15 mV and the pristine $MnO_2$/CC catalyst by 105 mV.[42] Vazhayil *et al.* synthesized a $NiCo_2O_4$/MXene electrocatalyst towards the OER by leveraging the advantageous features of integrating $NiCo_2O_4$ with MXene, such as synergistic effects, high surface area, and improved electronic conductivity. The synthesized /MXene composite achieved a low overpotential of 360 mV at a current density of 10 $mA\,cm^{-2}$, surpassing the performance of pure $NiCo_2O_4$, MXene, and their physically mixed counterpart.[43] Zhang *et al.* developed tremella-like Ni–NiO nanoarrays with oxygen vacancies grown in situ on $Ti_3C_2T_x$ MXene nanosheets, creating a highly effective bifunctional catalyst for water splitting. The Ni–NiO/ $Ti_3C_2T_x$ MXene exhibited the lowest overpotentials of 248 mV at 10 $mA\,cm^{-2}$ and 299 mV at 50 $mA\,cm^{-2}$, outperforming Ni–NiO, $Ni(OH)_2/Ti_3C_2T_x$ MXene, $NiO/Ti_3C_2T_x$ MXene, $Ni/Ti_3C_2T_x$ MXene and $IrO_2$.[44] Yan et al. enhanced OER activity by using $Ti_3C_2T_x$ MXene, which significantly promoted charge and mass transfer and hosted a large number of active sites on its surface, all while maintaining a strong coupling effect with Cr-FeNi-LDH. Chromium (Cr)-doping further increased the OER performance of FeNi LDH, leveraging the partial oxidation of $Cr^{3+}$ to $Cr^{6+}$ after the OER to facilitate the electron capture, charge transfer and active site stabilization. This modification led to the formation of Cr-FeNi LDH/ $Ti_3C_2T_x$ MXene nanocomposites with an overpotential of 232 mV at 10 $mA\,cm^{-2}$ and stable performance over 100 h in chronoamperometric measurements. The $Ti_3C_2T_x$ amount remained the same in the nanocomposites.[45] Hence, from the literature, it seems that there is a gap on the investigation and understanding of how various amounts of $Ti_3C_2T_x$ MXene effects the OER properties of Ni materials.

In this study, a composite material consisting of pure Ni oxide incorporated with varying $Ti_3C_2T_x$ contents (1–10%) was synthesized via a hydrothermal synthesis method. The electrochemical properties of all $NiO_x/Ti_3C_2T_x$ materials were analyzed to gain a deeper understanding of the MXene's role in the OER activity, stability, and Ni dissolution. The morphological and structural properties of all materials were examined using various characterization techniques, including operando Raman spectroscopy, to correlate real-time structural changes during the OER. The study demonstrates how the TMO/MXene ratio influences the OER activity of the active Ni material.

## Experimental Methods

### Chemicals and Materials

Sodium hydroxide (NaOH, 97+ %, ACS reagent) was purchased from Fisher Scientific. Nickel (II) nitrate hexahydrate ($Ni(NO_3)_2{\cdot}6H_2O$,

99.995 %), ethanol ($CH_3CH_2OH$, ≥ 99 %, reagent-grade), hydrochloric acid (HCl, 37 %) and lithium fluoride (LiF, 300 mesh) were purchased from Sigma-Aldrich. Nickel felt was purchased from Xinxiang AIDA Machinery Equipment Corporation, China. $Ti_3AlC_2$ MAX Phase (40 microns) was obtained from Carbon-Ukraine (Kiev). Ultra-pure water with a resistivity of 18.2 MΩ·cm$^{-1}$ was used in all experiments. All chemicals were used as received without further purification.

### MXene Synthesis

HF was generated in situ to etch the $Ti_3AlC_2$ MAX phase, resulting in the production of $Ti_3C_2T_x$. To achieve this, a solution of 10 ml of 9 M HCl and 1 g of LiF was stirred for 30 min at room temperature. $Ti_3AlC_2$ was then added stepwise to the mixture to avoid overheating. The etching reaction was carried out at 35 °C for 24 h. Afterwards, the acidic content was removed by washing with ultrapure water, followed by several centrifugation cycles at 3500 rpm for 5 min each. When the pH reached 7, delamination was initiated. The resulting slurry was collected, diluted, and sonicated during 1 h to achieve complete delamination. Finally, a centrifugation at 3500 rpm for 10 min was performed to collect the supernatant containing the delaminated $Ti_3C_2T_x$.

### Synthesis of Ni-Based Pure Materials and Ni/$Ti_3C_2T_x$ Composites

The pure $NiO_x$ and its $NiO_x/Ti_3C_2T_x$ composites were synthesized via a facile hydrothermal process. For the synthesis of $NiO_x/Ti_3C_2T_x$ composites, firstly, $Ni(NO_3)_2{\cdot}6H_2O$ (1 mmol) and urea (5 mmol) were dissolved in a water/ethanol solution (1 : 1) while stirring at room temperature. Then, varying amounts of MXene ($Ti_3C_2T_x$) suspensions, corresponding to the molar mass percentages of 1 %, 5 % and 10 %, were added to the Ni solution. The pH was adjusted by adding 1 mL of 1 M NaOH. The resulting suspension was transferred into a 23 ml Teflon-lined stainless-steel autoclave and heated at 150 °C for 3 h. The mixture was allowed to cool down to room temperature naturally, followed by washing with ultrapure water (4x11 mL) and absolute ethanol (4x11 mL). Finally, the product was dried overnight in an oven at 60 °C. The synthesized $NiO_x/Ti_3C_2T_x$ composites were labelled as $NiO_x$/1 %$Ti_3C_2T_x$, $NiO_x$/5 %$Ti_3C_2T_x$, and $NiO_x$/10 %$Ti_3C_2T_x$ according to the $Ti_3C_2T_x$ molar mass percentages of 1, 5 and 10 %, respectively. For the synthesis of the pure material, the same procedure was followed, but without the addition of $Ti_3C_2T_x$.

### Materials Characterization

Powder X-ray diffraction analyses were performed using a Bruker D8 Advanced diffractometer with CuKα radiation (λ = 0.1541 nm). Diffraction data were recorded between 5° and 90° 2θ range with a step size of 0.0131° and a step time of 1.5 seconds. All samples were measured in their powdered form. Scanning electron microscopy (SEM) analyses were conducted to study the catalyst morphologies using a ZEISS Gemini SEM 460, a field emission gun scanning electron microscope operating at 0.1–30 keV. For all SEM studies, the reaction products were used in powder form and dried at 60 °C for 1 h before the measurement. The energy-dispersive X-ray spectroscopy (EDX) was also performed to reveal elemental distributions of the materials using an Oxford Instruments Ultim Extreme EDX detector with an accelerating voltage of 3 kV. AZtecLive software was used to identify the elemental distribution peaks.

Operando Raman spectroscopy measurements were conducted using an i-Raman Plus 532H portable spectrometer (532 nm laser) in combination with a PalmSens electrochemical workstation. For potential-dependent operando Raman analysis, a magnetic-mount Raman electrochemical flow cell (Raman ECFC 3.5 cm$^2$, Redox.me) was used with 4.5 ml of 1 M NaOH solution as the electrolyte. The catalyst was drop-cast onto the surface of a gold sample holder, serving as electric contact to the working electrode. Chronoamperometry was performed at applied potentials ranging from 1.30 V to 1.65 V vs. RHE during operando Raman measurements. Each applied potential was maintained for 30 seconds before collecting a series of 5 Raman spectra over a period of 5 min.

X-ray photoelectron spectroscopy (XPS) measurements were conducted using a JEOL JPS-9030 setup with a base pressure of $2{\cdot}10^{-9}$ mbar. The powders were distributed evenly on carbon tape. A non-monochromated Al source with 300 W power was used for excitation and a hemispherical analyzer with pass energies of 50 eV (surveys) and 20 eV (narrow scans) was used to detect the emitted photoelectrons, yielding a resolution of 1.2 eV as estimated from the width of the $Ag3d_{5/2}$ peak of a silver foil. The analyzer binding energy scale was calibrated by measuring sputter cleaned gold and copper foils just before the measurements and setting the $Au4f_{7/2}$ peak to 84.00 eV and the $Cu2p_{3/2}$ peak to 932.62 eV. Since the samples exhibited charging, we've set the binding energy of the O1s peak to 532.0 eV for comparison. CasaXPS was used for peak fitting.[46] Inductively coupled plasma optical emission spectroscopy (ICP-OES) measurements were performed using an iCAP 7400 Duo Full MFC device (Thermo Fisher Scientific) in axial mode.

### Electrochemical Measurements

Electrochemical measurements were performed using a standard three-electrode configuration. The setup consisted of a carbon rod as the counter electrode, a standard mercury–mercury oxide (Hg/HgO) reference electrode and a glassy carbon (GC) disc electrode with a surface area of 0.0707 cm$^2$ serving as the working electrode. The system was coupled with a rotating ring disc electrode (RRDE-3 A, Ver 3.0, ALS-Japan) setup and the measurements were carried out using an electrochemical workstation (VIONIC, Metrohm Autolab or PalmSens). 1 M NaOH electrolyte was saturated with $N_2$ for over 20 min to remove dissolved oxygen and was used as the electrolyte. A catalyst ink was prepared for each material by using the following procedure: 10 mg of catalyst was dispersed in 1 mL of a 1 : 1 solution of water and isopropanol and 8 μL of Nafion solution, and then sonicated for 15 min in an ultrasonic bath. The prepared ink was drop-cast onto the polished GC electrode surface and dried at room temperature, achieving a mass loading of 0.32 mg cm$^{-2}$.

Cyclic voltammetry (CV) and linear sweep voltammetry (LSV) measurements were conducted at scan rates of 40 mV s$^{-1}$ and 1 mV s$^{-1}$, respectively. The iR-drop correction was performed for all presented data by measuring the solution resistance with potentiostatic electrochemical impedance spectroscopy (PEIS) at non-Faradaic potential over a frequency range of 1 MHz to 1 Hz with a perturbation of 10 mV. The double layer capacitance was measured by recording multiple CVs in a scan range of 100 mV in non-Faradaic region at scan rates ranging from 1 to 100 mV s$^{-1}$. The recorded currents were plotted against the scan rate to obtain a slope that was used to calculate the double layer capacitance. To estimate the electrochemically active surface area (ECSA), a general specific capacitance value of 40 μF cm$^{-2}$ was used based on typical reported values for transition metals in 1 M NaOH.[47] For the long-term stability tests, chronopotentiometry (CP) was conducted at constant currents of 10 mA cm$^{-2}$ and 100 mA cm$^{-2}$ for 12 h, respectively. All measured potentials (vs. Hg/HgO) were converted

to the reversible hydrogen electrode (RHE) according to the Nernst equation:

$$E_{RHE} = E_{Hg/HgO} + 0.059\ pH + E^{0}_{Hg/HgO} \quad (1)$$

where $E_{Hg/HgO}$ is the standard potential of the Hg/HgO electrode, which is 0.098 V at 25 °C.

## 2. Results and Discussion

In this study, $NiO_x$ and $NiO_x/Ti_3C_2T_x$ materials were synthesized using a facile urea-assisted hydrothermal approach, as illustrated in Figure 1. First, $Ti_3C_2T_x$ MXene was prepared by selectively etching the aluminum layer from $Ti_3AlC_2$ through a in situ HF method, followed by exfoliation through sonication for 1 h to obtain delaminated $Ti_3C_2T_x$. Subsequently, the synthesis of $NiO_x/Ti_3C_2T_x$ composites was performed by incorporating the required amount of $Ti_3C_2T_x$ (1 to 10% mass percentages) into a Ni-containing precursor solution, followed by hydrothermal treatment at 150 °C for 3 h in an autoclave. For comparison, pure $NiO_x$ was also synthesized under the same conditions. Detailed synthesis procedures are provided in the experimental section. Hereafter, the composite synthesized with $Ti_3C_2T_x$ will be referred to as, $NiO_x/1\%Ti_3C_2T_x$, $NiO_x/5\%Ti_3C_2T_x$, and $NiO_x/10\%Ti_3C_2T_x$ while the pure material is designated as $NiO_x$.

The morphological characteristics and elemental distributions of the catalysts were analyzed via SEM-EDX, as shown in Figure 2. Top-view SEM images and elemental mapping analyses confirmed the successful synthesis of the bare $NiO_x$ and $Ti_3C_2T_x$ MXene through hydrothermal synthesis and chemical etching, respectively. $NiO_x$ exhibited a flower-like structure composed of nano-petals as shown in Figure 2a, while $Ti_3C_2T_x$ in Figure 2b, displayed the desired delaminated structure, resulting from the overlaying of nanolayers during drying, with the absence of the typical accordion-like microstructure seen in multi-layered MXenes. The $NiO_x/Ti_3C_2T_x$ materials incorporating 1%, 5% and 10% of $Ti_3C_2T_x$ MXenes showed the presence of the chemically functionalized MXenes nanosheets, characterized by their rough surface texture, Figure 2c–e. Elemental mapping confirmed the presence of nickel and oxygen as shown in Figure 2f–j. At higher $Ti_3C_2T_x$ loadings, increased Ni and O particle agglomeration was observed.

X-ray diffraction analysis was performed on the catalysts, both pure and composite forms, to identify the present phases and examine how the addition of $Ti_3C_2T_x$ to $NiO_x$ affected the crystal structure. The diffraction patterns of the prepared materials are shown in Figure 3. For the $NiO_x$ sample, all observed peaks match those of α-$Ni(OH)_2$ (PDF: 22–0444), as depicted in Figure 3a.[48] When $Ti_3C_2T_x$ was introduced to form the $NiO_x/Ti_3C_2T_x$ composites, the $NiO_x$ diffraction peaks underwent noticeable changes. The resulting patterns indicated that α-$Ni(OH)_2$ transformed into β-$Ni(OH)_2$ (ICSD: 169978) within the composite structure.[49]

The $Ti_3C_2T_x$ MXene pattern displayed characteristic peaks at 6°, 14°, 28°, 35°, and 43°, consistent with previously reported data (Figure 3b).[50] In the $NiO_x@1\%Ti_3C_2T_x$ sample, the (002) peak is not detectable due to the dominant $NiO_x$ signals and the small amount of $Ti_3C_2T_x$ present. However, this peak becomes visible in composites with higher $Ti_3C_2T_x$ content (5%, and 10%). Furthermore, in these samples, the peak shifts towards lower 2θ angles compared to pristine $Ti_3C_2T_x$, suggesting that $NiO_x$ has been incorporated and the distance between MXene layers has increased (Figure 3c). Furthermore, there was no detection of $TiO_2$ in the bulk of the sample from the XRD.

X-Ray photoelectron spectroscopy (XPS) measurements were conducted to identify the chemical states of the nickel and titanium composites and to determine the elemental composition at the surface of the samples. Figure 4a shows the Ni2p core levels of the $NiO_x$ samples with different amounts of $Ti_3C_2T_x$ added. Nickel is present as $Ni(OH)_2$ for all samples, as can be deducted from the line shape of the core level and the Ni LMM Auger spectra (Supplementary Information, Figure S2 and an Auger parameter of 1698.21 eV.[51] The addition of any amount of $Ti_3C_2T_x$ does not alter the Ni2p spectra, indicating no chemical interaction between the $Ti_3C_2T_x$ and the $NiO_x$. Figure 4b shows the Ti2p core levels for different amounts of

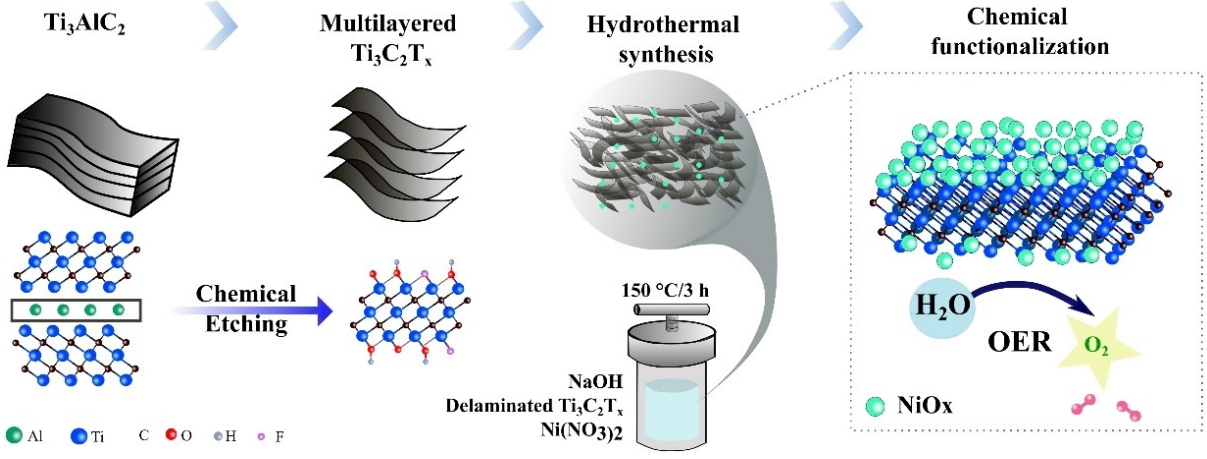


**Figure 1.** Schematic of synthesis procedure of $NiO_x/Ti_3C_2T_x$ composites.

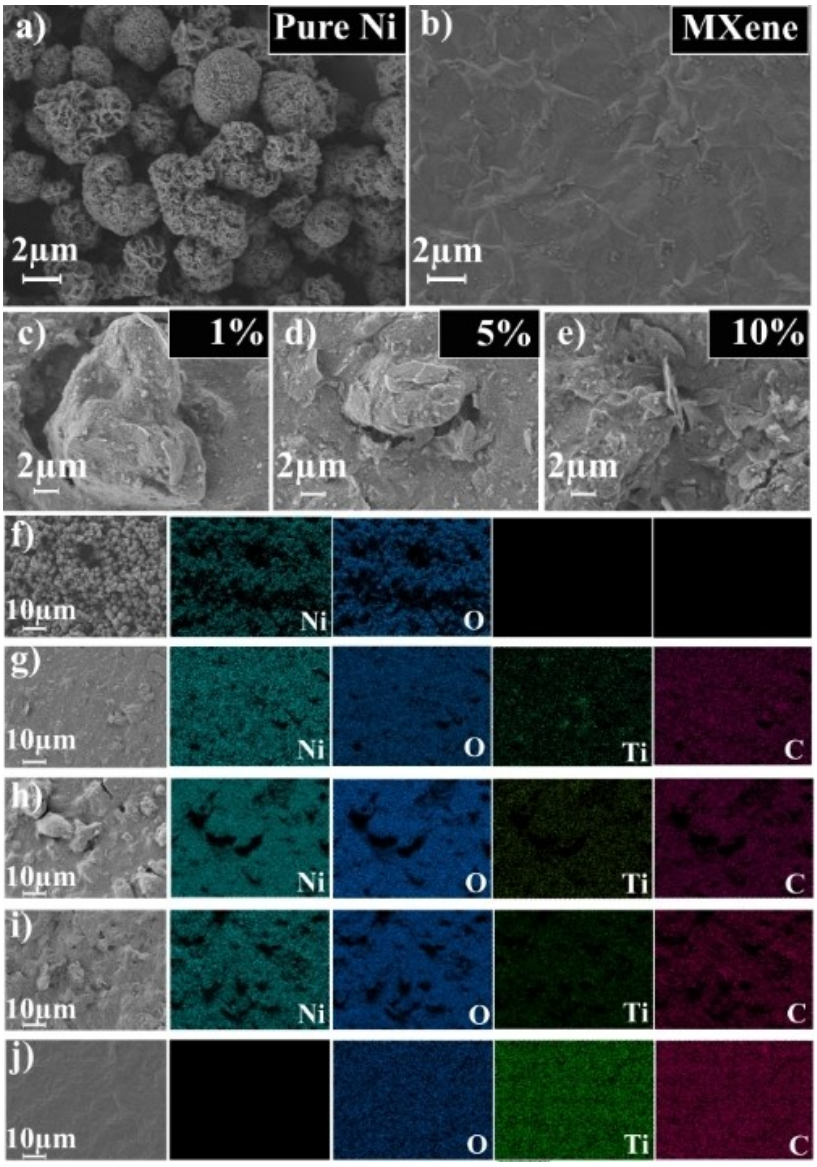


**Figure 2.** Scanning electron microscope images of a) pure $NiO_x$, b) pure $Ti_3C_2T_x$ MXene, c) $NiO_x$/1 %$Ti_3C_2T_x$, d) $NiO_x$/5 %$Ti_3C_2T_x$, e) $NiO_x$/10 %$Ti_3C_2T_x$, and energy dispersive x-ray mapping images of f) pure $NiO_x$, g) $NiO_x$/1 %$Ti_3C_2T_x$, h) $NiO_x$/5 %$Ti_3C_2T_x$, i) $NiO_x$/10 %$Ti_3C_2T_x$, and j) pure $Ti_3C_2T_x$ MXene.

$Ti_3C_2T_x$. Notably there is some satellite intensity also for the samples nominally not containing any $Ti_3C_2T_x$, whose origin is unknown. This must be considered when fitting the samples actually containing $Ti_3C_2T_x$, due to the low amount added. Besides the satellite background intensity, the Ti2p spectrum consists of two contributions. One doublet (blue) corresponding to $TiO_2$ and one doublet (red) corresponding to non-oxidized $Ti_3C_2T_x$. Although the $Ti_3C_2T_x$ spectra is typically fitted using multiple peaks[52] we used a simplified model of only one pair of peaks due to the low intensity. The overall Ti/Ni ratio follows the nominally added $Ti_3C_2$ amount, as shown in Figure 4c. For low amounts of $Ti_3C_2T_x$ (1 %) almost all the MXene is oxidized. For higher amounts of $Ti_3C_2T_x$ added, more of the MXene remains intact, as summarized in Figure 4d. Hence, unlike the bulk of the sample where no $TiO_2$ is detected by XRD, Figure 3, $TiO_2$ is clearly present on the surfaces of the composites with varying amounts depending on the $Ti_3C_2T_x$ content. Recently, Buldu-Akturk and co-workers showed that the oxidation of the MXene could play a role in the changing (reduction) of the metal oxide in the MXene composite materials.[53] Interestingly, in this current study, no reduction of the Ni is observed however, from the XRD there is a phase change from alpha to beta $Ni(OH)_2$ on addition of the MXene.

### 2.2. Electrochemical Characterization

The electrocatalytic OER performances of the pure $NiO_x$ and its $Ti_3C_2T_x$ MXene composites were evaluated in 1 M NaOH electrolyte. To assess the materials' OER activity, LSV measurements were conducted, focusing particularly on the overpotential

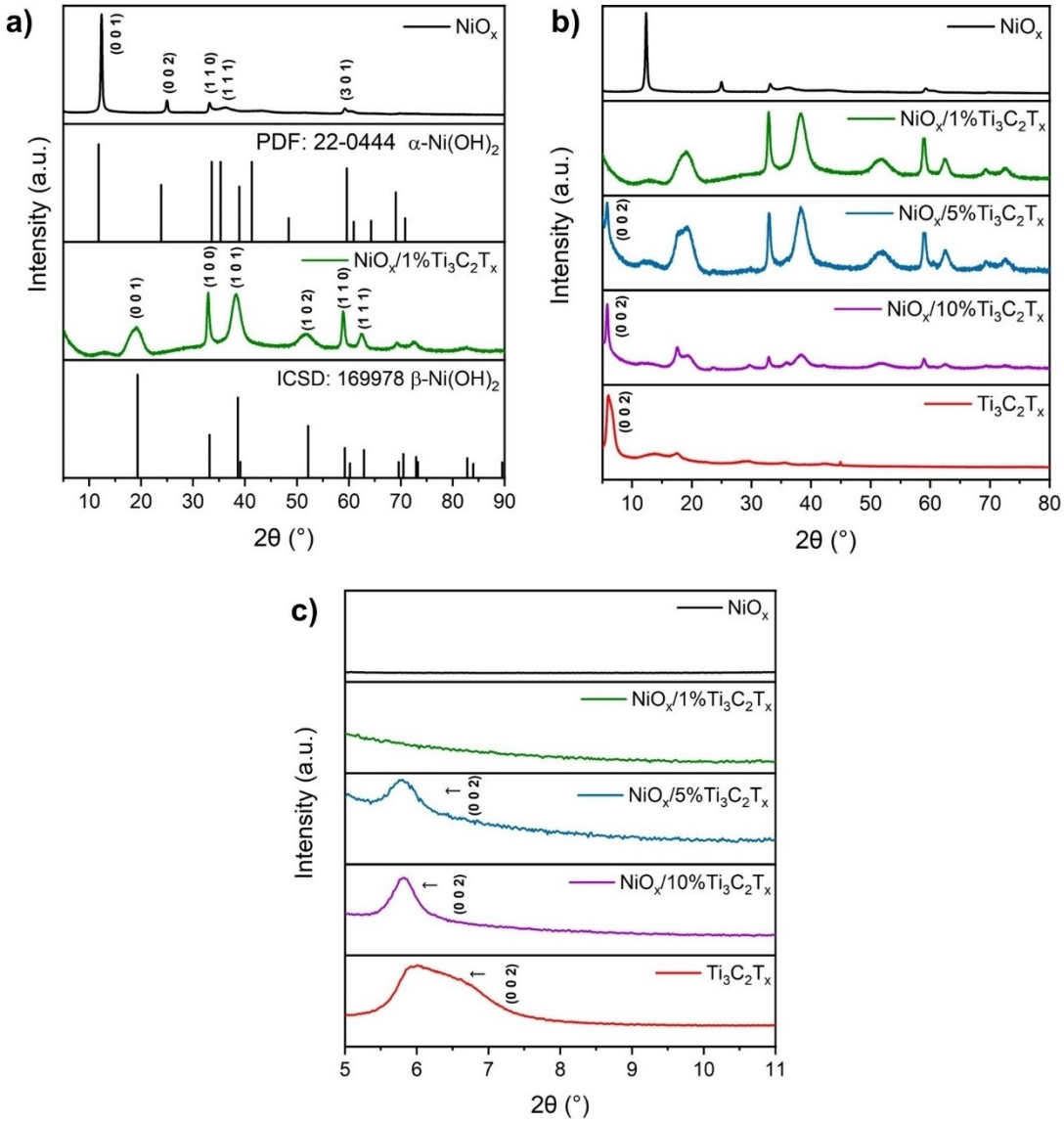


**Figure 3.** X-ray diffraction (XRD) patterns of $NiO_x$ and $NiO_x/Ti_3C_2T_x$ composites with varying $Ti_3C_2T_x$ content (1%, 5%, and 10% by mass). a) pure NiOx and $NiO_x$/1%$Ti_3C_2T_x$ with reference spectra, b) pure $NiO_x$, pure $Ti_3C_2T_x$, and $NiO_x/Ti_3C_2T_x$ composites, and (c) a zoomed-in view of the XRD patterns from (b) for the 2θ range of 5-11°.

required to achieve the benchmark current density of 10 mA cm$^{-2}$ ($\eta_{10}$), which serves as a key performance indicator.

As shown in Figure 5a, the geometric area-normalized current density was plotted against the overpotential for all materials, with the corresponding $\eta_{10}$ values and error bars in Figure 5b. A significant reduction in overpotential is observed for all MXene-containing materials when compared to the pure $NiO_x$ material. The $NiO_x$/1%$Ti_3C_2T_x$ composite exhibited the lowest overpotential of 354 mV, followed by $NiO_x$/5%$Ti_3C_2T_x$ at 396 mV and $NiO_x$/10%$Ti_3C_2T_x$ at 434 mV. In contrast, the pure $NiO_x$ material exhibited a significantly higher overpotential, indicating that the integration of $Ti_3C_2T_x$ effectively enhances the OER activity of the composite catalysts. Meanwhile the pure $Ti_3C_2T_x$ MXene showed very poor OER capabilities in the same potential window. Furthermore, to determine if a lower molar mass % of $Ti_3C_2T_x$ would be better than the 1% composite, a 0.5% was synthesized and characterized by SEM-EDX and XRD, Figure S1. The SEM-EDX exhibits a similar morphology to the other composites, Figure S1 A–B. The $NiO_x$/0.5%$Ti_3C_2T_x$ XRD pattern was similar to that of the $NiO_x$/1%$Ti_3C_2T_x$, but without an obvious $Ti_3C_2T_x$ (002) peak, as presented in Figure S1C. The LSV, Figure S1D, of the $NiO_x$/0.5%$Ti_3C_2T_x$ exhibits poorer OER capabilities than the $NiO_x$/1%$Ti_3C_2T_x$, which could be due to the lower amount of MXene in the composite, evident by the XRD.

The ECSA was determined by measuring the double-layer capacitance (DLC) of each material and dividing it by the specific capacitance ($C_s$) for transition metals in 1 M NaOH, which is typically set at 40 μF cm$^{-2}$.[47] The ECSA-corrected LSV curves and corresponding overpotentials ($\eta_{10}$) are depicted in Figure 5c and d, respectively. ECSA-correction confirmed an improved OER performance for the $NiO_x/Ti_3C_2T_x$ composites, particularly for those with lower $Ti_3C_2T_x$ content. However, it

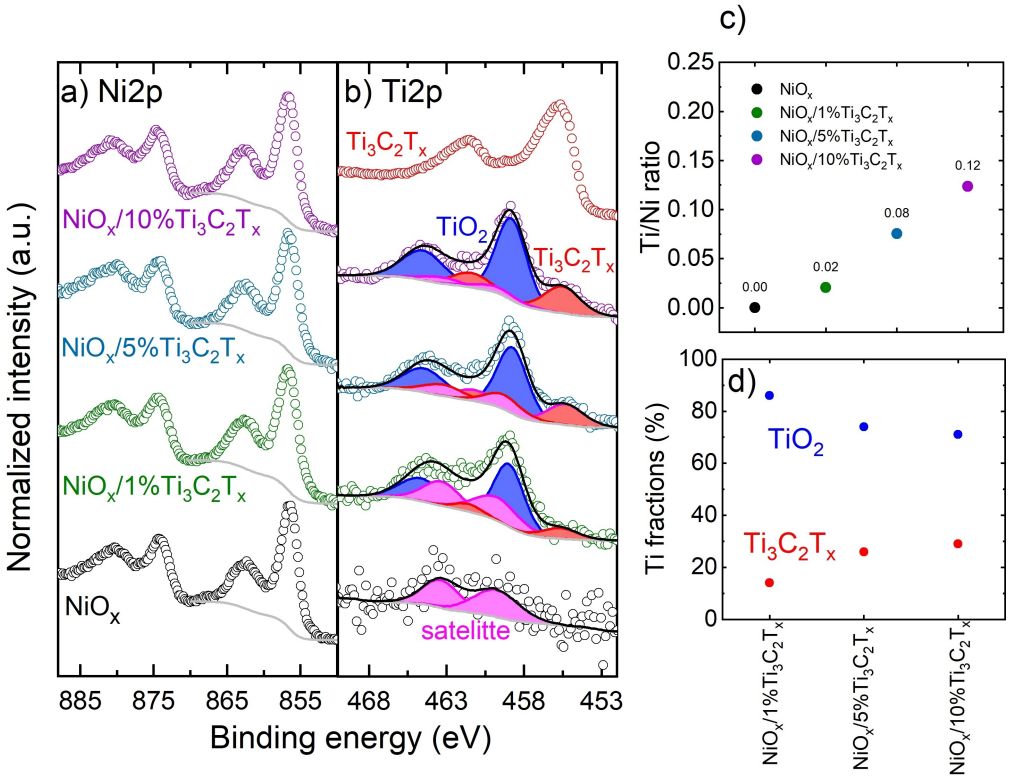


**Figure 4.** X-Ray photoelectron spectroscopy results of the $NiO_x$ samples with different amounts of $Ti_3C_2T_x$. a) Ni2p core levels, b) Ti2p core levels, c) Ti/Ni ratio and d) $TiO_2$ and $Ti_3C_2T_x$ contributions in the Ti2p core levels.

was also observed that the addition of 10% $Ti_3C_2T_x$ leads to a higher overpotential compared to the pure $NiO_x$, indicating a reduction in the number of electrochemically active sites. Again, for comparison, it was shown that the pure MXene exhibited no activity towards OER in all cases.

To evaluate the catalytic efficiency and the reaction kinetics of the prepared catalysts, Tafel slopes were calculated for the overpotentials at 10 mA cm$^{-2}$ and are presented in Figure 6a. A similar trend for the Tafel slopes was observed as in Figure 6b for the overpotentials at 10 mA cm$^{-2}$. Both the pure $NiO_x$ and the composite with highest MXene content exhibited Tafel slope values of 81 and 82 mV dec$^{-1}$, respectively, while significantly shallower slopes were obtained for $NiO_x$/5%$Ti_3C_2T_x$ (64 mV·dec$^{-1}$) and $NiO_x$/1%$Ti_3C_2T_x$ (54 mV·dec$^{-1}$). This trend suggests that finding the optimum MXene content is important, as lower MXene content in the composites leads to more favorable reaction kinetics and a faster OER rate.

Further insight into catalytic performance can be gained by considering another key activity metric, the catalytic turnover frequency (TOF). The TOF values reveal a deeper understanding of the efficiency of the catalyst by quantifying its ability to produce oxygen per active site per unit of time. The TOF values are calculated using the equation $TOF = j_E/(4Q)$, where $j_E$ is the voltammetric charge density calculated from the anodic peak of the material, Q is the current density at a specific potential associated with OER (typically 350 mV vs RHE), and the factor 4 represents the number of electrons that are transferred per oxygen molecule generated.[54] The TOF values of all materials are depicted in Figure 6b. The highest TOF values are observed for $NiO_x$/1%$Ti_3C_2T_x$, followed by $NiO_x$/5%$Ti_3C_2T_x$, while the lowest values are obtained for $NiO_x$/10%$Ti_3C_2T_x$ and pure $NiO_x$, reflecting their relatively lower OER activity. These results follow a similar trend and correlate well with the overpotentials at 10 mA cm$^{-2}$ presented in Figure 5 and Tafel slopes shown in Figure 6a.

The long-term stability of the prepared catalysts was tested using chronopotentiometry for 12 h at a constant current density of 10 mA cm$^{-2}$, Figure 6c. The catalyst inks were spray-coated onto the surface of the Ni felts with 1 cm$^2$ area, as it is important to scale-up OER materials and analyze them on industrial relevant electrodes. The first notable observation is the stable curve trends observed for $NiO_x$/1%$Ti_3C_2T_x$ and pure $NiO_x$, highlighting their excellent stability with negligible or improved changes in their overpotentials over the testing period. Notably, $NiO_x$/1%$Ti_3C_2T_x$ maintained the lowest overpotential of 276 mV after 12 h. Hence, the lower overall Ti:Ni ratios, Figure 4c, produces the better OER MXene composites when combined with the Ni oxide. On the other hand, $NiO_x$/10%$Ti_3C_2T_x$ exhibited the largest increase in overpotential, hence worse stability. This loss in stability for the materials with a higher amount of $Ti_3C_2T_x$ could be due to the formation of increasing $TiO_2$ during the OER which may decrease OER activity. $TiO_2$ is known to be an insulating material therefore increasing $TiO_2$ in a film could lead to the decreased flow of electrons which could slow down the OER process. As there is a higher amount of MXene in the 5 and 10% composites, this

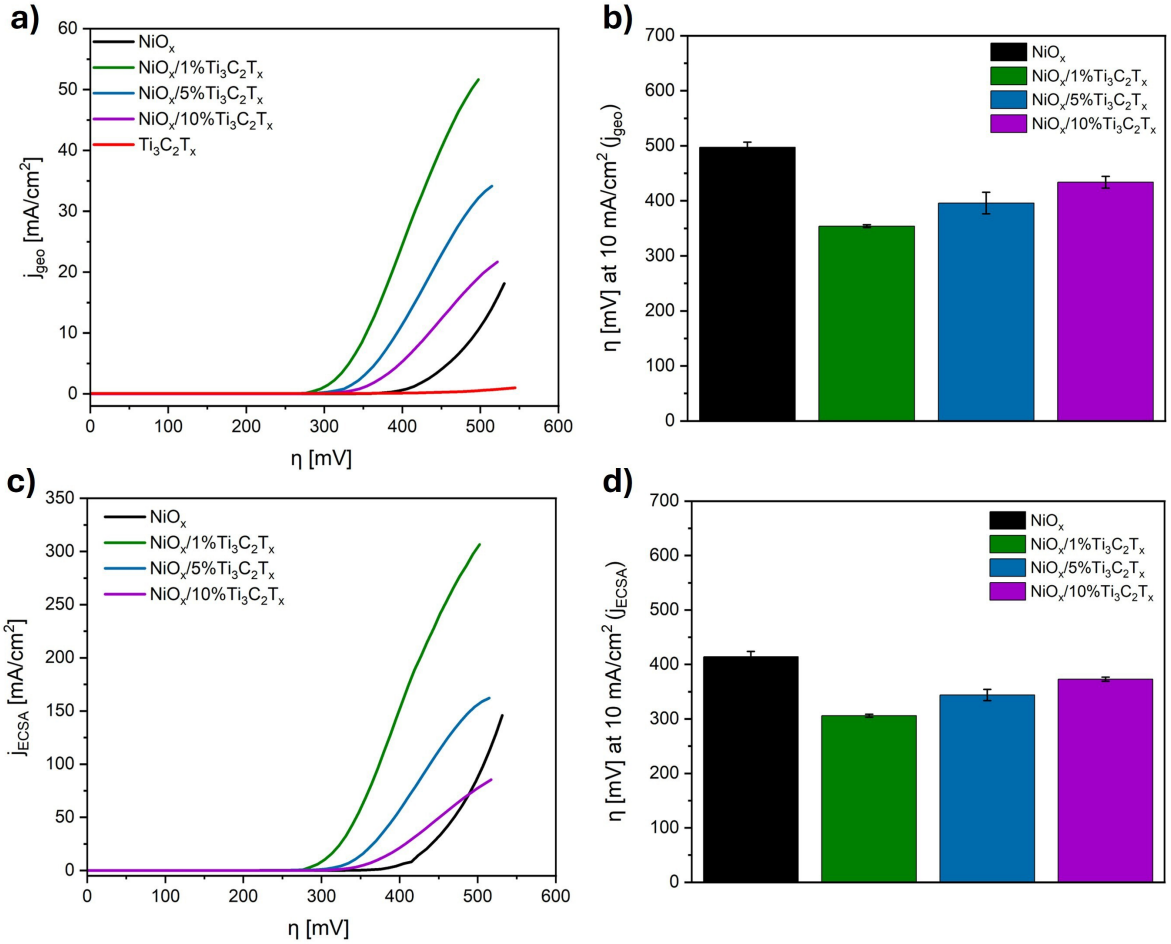


**Figure 5.** Electrochemical evaluation of $Ti_3C_2T_x$, pure $NiO_x$ and chemically functionalized $NiO_x/Ti_3C_2T_x$ composites with different concentrations of $Ti_3C_2T_x$ towards OER: a) iR-corrected geometric area-normalized LSV curves, b) corresponding geometric area-normalized $\eta_{10}$ values, c) ECSA-normalized LSV curves, d) corresponding ECSA-normalized $\eta_{10}$ values.

means there is more reactant for $TiO_2$ to form during the OER. In particular, for the $NiO_x/10\%Ti_3C_2T_x$ catalyst, the increased amount of $TiO_2$ could even block Ni-$Ti_3C_2T_x$ active sites leading to this catalyst exhibiting worse OER capabilities than the pure $NiO_x$ material, with all its Ni sites available for the OER.

The stability of the catalysts was further evaluated at a higher current density of 100 mA cm$^{-2}$ for 12 h to assess their performance under more industrially relevant conditions, as shown in Figure 6d. The trends observed at 100 mA·cm$^{-2}$ were similar to those from the 10 mA cm$^{-2}$ tests, reinforcing the reliability of the results. $NiO_x/1\%$ $Ti_3C_2T_x$ exhibited the best stability, maintaining the lowest overpotential of 341 mV after 12 h. Pure $NiO_x$ and $NiO_x/5\%$ $Ti_3C_2T_x$ displayed comparable overpotentials of approximately 420 mV after 12 h, although the 5% composite appeared slightly more unstable based on the progression of the curve. $NiO_x/10\%Ti_3C_2T_x$ exhibited the poorest stability, with its overpotential rising to 450 mV by the end of the test, indicating that excessive MXene content negatively impacts long-term performance. These results emphasize that a balanced incorporation of $Ti_3C_2T_x$ is critical for achieving high stability, as excessive MXene promotes the formation of $TiO_2$ during OER, which acts as an insulating phase and blocks active sites.

### 2.3. Operando Raman Spectroscopy

This research utilized operando Raman spectroscopy measurements on the $NiO_x$ and $NiO_x/1\%Ti_3C_2T_x$ samples, collecting Raman spectra at different electrical bias points to monitor the surface bonding changes and catalyst phase evolution during OER operation, as presented in Figure 7. The analysis of the spectra revealed a consistent peak at approximately 416 cm$^{-1}$ across all potentials, which was attributed to the gold electrode substrate.

In the case of the pure $NiO_x$ film, the initial spectrum without applied potential exhibited a main band at 490 cm$^{-1}$, typical of $Ni(OH)_2$ $A_{1g}$ vibrations, Figure 7a.[55] As the potential reached 1.55 V vs. RHE, a transformation from α-$Ni(OH)_2$ to β-NiOOH was observed, evidenced by the appearance of characteristic double peaks around 475 and 555 cm$^{-1}$, with the latter peak being of greater intensity. These peaks correspond to Ni–O bending and stretching vibrations, respectively, and their

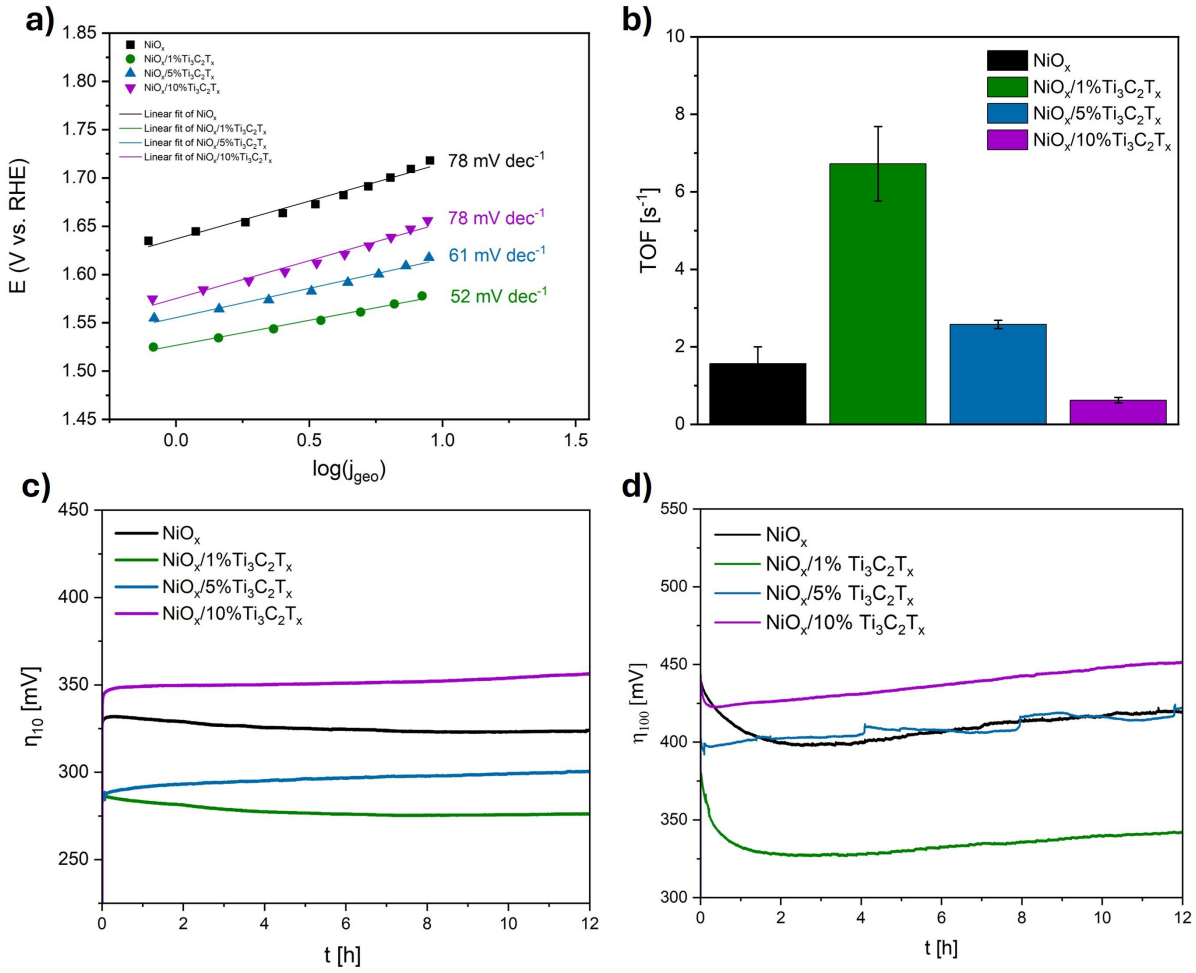


**Figure 6.** The catalytic efficiency of the pure $NiO_x$ and $NiO_x$/1 %$Ti_3C_2T_x$, $NiO_x$/5 %$Ti_3C_2T_x$, and $NiO_x$/10 %$Ti_3C_2T_x$ composites: a) Tafel slopes, b) TOF bar charts with error bars, and chronopotentiometric stability curves at constant current densities of c) 10 mA cm$^{-2}$ and d) 100 mA cm$^{-2}$ for 12 h.

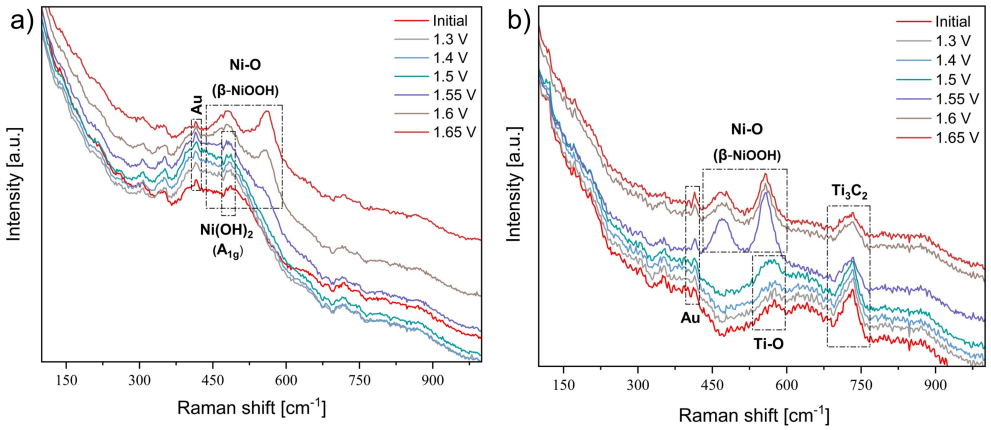


**Figure 7.** Operando Raman spectra of the a) $NiO_x$ and b) $NiO_x$/1 %$Ti_3C_2T_x$ composites during the OER with a potential sweep ranging from 1.3 V to 1.65 V vs. RHE.

positions are in agreement with previous reports.[56,57] The signals remained stable during operando measurements at 1.65 V vs. RHE, suggesting no further changes in the catalyst and indicating β-NiOOH as the active species for OER.

For the $NiO_x$/1 %$Ti_3C_2T_x$ sample, the initial spectrum without applied potential showed primary bands at 576 and 733 cm$^{-1}$, which are associated with the typical $E_{g(3)}$ vibrations of Ti–O bonds and the vibrational modes of $Ti_3C_2T_x$, Figure 7b.[58] The presence of a peak related to the Ti–O bond in this sample

indicates partial oxidation of $Ti_3C_2T_x$ during the hydrothermal process already detected by the XPS. Notably, in this sample, the β-NiOOH double peaks appeared at a lower potential (compared to $NiO_x$) of 1.5 V vs. RHE, suggesting that the modified catalyst surface requires less energy for β-NiOOH formation.

The operando Raman spectroscopy in this study suggests that $Ti_3C_2T_x$ enhances β-NiOOH formation through multiple synergistic effects. First, $Ti_3C_2T_x$ exhibits electron-withdrawing characteristics[59] that alter the electronic structure of adjacent $NiO_x$ sites. At the interface, strong Ti–O interactions redistribute electron density, generating nickel centers with increased electrophilicity that favor the nucleophilic addition of water molecules - a critical initial step in the catalytic cycle.[27,60,61] Such electronic tuning lowers the energy threshold for converting Ni(II) to Ni(III), which explains the observed β-NiOOH formation at reduced potentials. Furthermore, the abundant surface terminations on $Ti_3C_2T_x$ sheets can serve as proton acceptors,[62] facilitating the deprotonation steps necessary for β-NiOOH formation.[63] This enhanced proton mobility across the catalyst surface substantially decreases the energy needed for Ni(II)/Ni(III) transition. In addition, the intimate contact between $NiO_x$ and $Ti_3C_2T_x$ may create interfacial sites with modified local coordination environments,[64] potentially offering lower-energy pathways for structural reorganization during the phase transition to β-NiOOH. The electronic modulation and enhanced proton transfer kinetics provide a solid framework for understanding the lower energetic requirements for β-NiOOH formation in the $NiO_x$/1 % $Ti_3C_2T_x$ composite.

### 2.4. The Role of MXene on the Dissolution Behavior of the Catalysts

ICP-OES analyses were performed on the pure $NiO_x$ and its $Ti_3C_2T_x$ MXene composites after the stability tests at a constant current density of 10 mA·cm$^{-2}$, as shown in Figure 8. The results revealed that Ni leaching into the electrolyte was evident for pure $NiO_x$, whereas no Ni leaching was observed for its $NiO_x$/1 % $Ti_3C_2T_x$, $NiO_x$/5 %$Ti_3C_2T_x$, and $NiO_x$/10 %$Ti_3C_2T_x$ composites. This indicates that the incorporation of $Ti_3C_2T_x$ enhances the structural stability of $NiO_x$ in alkaline conditions, preventing Ni dissolution during operation, which also improves the OER activity of these MXene composite materials.

For the composites the leaching behavior was found to depend on the MXene content. Composites with higher

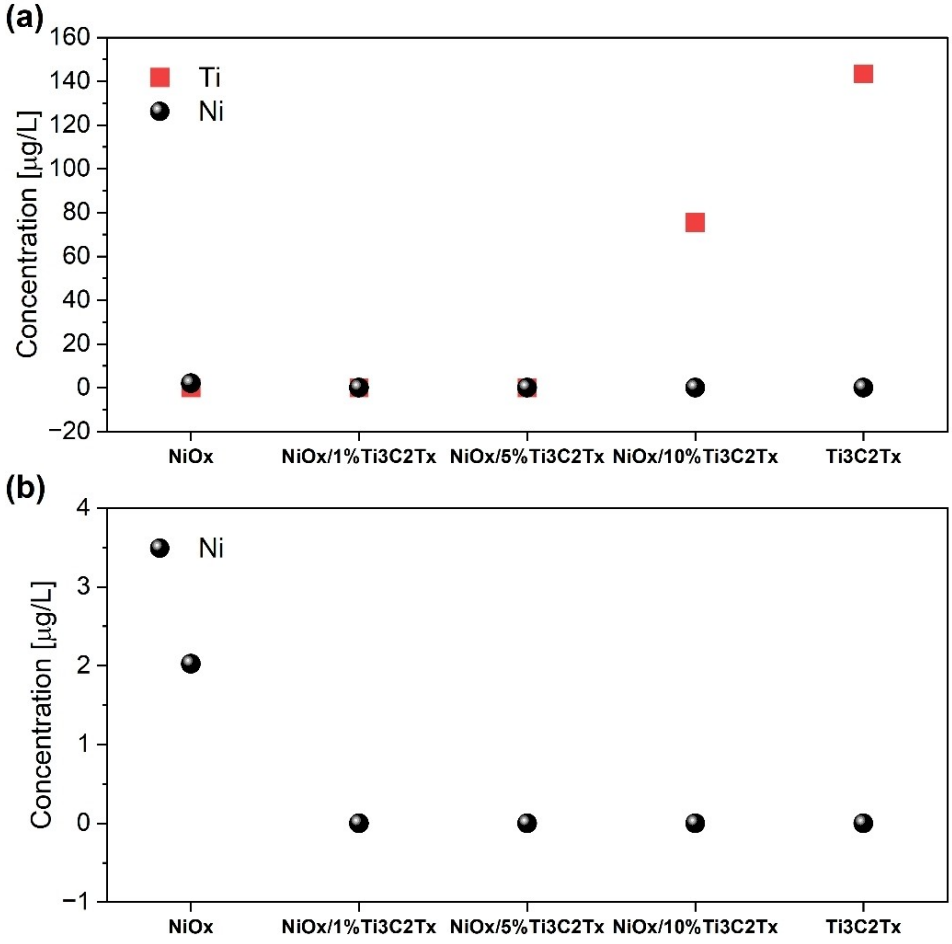


**Figure 8.** (a) Concentration of Ni and Ti in the electrolytes after stability tests measured by ICP-OES analysis, (b) a zoomed-in view of the y-axis from (a), emphasizing the zero concentration of Ni for clearer visualization.

concentrations of $Ti_3C_2T_x$ exhibited more pronounced Ti leaching, suggesting that the Ti phase from MXene component is preferentially leached from the material, especially at high concentrations, while Ni remains stable (Figure 8a and b). This could be linked to unreacted $Ti_3C_2T_x$ not bond to Ni for the higher MXene content, as Ti leaching likely leads to the formation of inactive $TiO_2$, thereby reducing the overall catalytic activity of the material. These findings revealed the role of $Ti_3C_2T_x$ MXene on mitigating Ni leaching in alkaline conditions and highlighted the importance of optimizing the $Ti_3C_2T_x$ content to balance performance and durability for long-term OER applications.

## 3. Conclusions

In this study, we investigated and tried to elucidate the role of MXene concentration in enhancing the OER performance of $NiO_x$ catalysts. $NiO_x/Ti_3C_2T_x$ MXene composites were synthesized with varying $Ti_3C_2T_x$ contents (1–10%) through a hydrothermal synthesis method. The structural and morphological information of the synthesized pure and composite materials was collected through SEM-EDX, XRD and XPS. The pure Ni material was made of $\alpha$-$Ni(OH)_2$ while upon MXene addition the phase changed to $\beta$-$Ni(OH)_2$. Additionally, the results show that $TiO_2$ is present on the surface of all materials but not in the bulk, which was still $Ti_3C_2T_x$. Furthermore, the MXene content affects the amount of $TiO_2$ and $Ti_3C_2T_x$, with the lower MXene contents exhibiting less MXene at the surface.

Our findings from the electrochemical measurements reveal that MXene not only improves the exposure of active sites but also facilitates electron transfer, which leads to significant enhancement in the OER catalytic activity. The optimal MXene concentration was determined to be 1%, with performance declining at higher concentrations. This trend indicates that identifying the optimal MXene content is crucial, as lower MXene content in the composites results in more favorable reaction kinetics and a faster OER rate. Furthermore, the structural evolution of the pure $NiO_x$ and the best performing composite, $NiO_x/1\%Ti_3C_2T_x$, was investigated through operando Raman measurements. It was determined that $\beta$-NiOOH was the active phase for OER, and that the $Ti_3C_2T_x$ has a positive impact on facilitating proton transfer at the catalyst surface, accelerating deprotonation and critical intermediate formation. Finally, $NiO_x/1\%Ti_3C_2T_x$ exhibited the lowest overpotential of 276 mV after 12 h, indicating excellent long-term stability with no Ni leaching, as shown by the ICP-OES analyses. These results demonstrate the positive effect of $Ti_3C_2T_x$ incorporation in elevating the OER activity and stability of Ni-based OER catalysts, offering a promising alternative for the development of efficient novel electrocatalysts for sustainable hydrogen production.

## Acknowledgements

We gratefully acknowledge the Helmholtz Association's Initiative and Networking Fund (Helmholtz Young Investigator Group VH-NG-1719) for the funding. M.P.B and A.A.E greatly acknowledges support from the German Federal Ministry of Education and Research in the framework of the project Catlab (03EW0015 A/B). The authors would like to address particular thanks to R. Schwiddessen, M. Tovar and K. Schwarzburg from the X-Ray and Microscopy and Spectroscopy corelabs of the Helmholtz Zentrum Berlin for providing access to their facility and training on the equipment. The ICP-OES measurements were carried out by the "Solar Fuels Testing Facility" laboratory of the Helmholtz Energy Materials Foundry (HEMF) and we thank Ursula Michalczik and Dr. Peter Bogdanoff for performing these measurements. Open Access funding enabled and organized by Projekt DEAL.

## Conflict of Interests

The authors declare no conflict of interest.

## Data Availability Statement

The data that support the findings of this study are available from the corresponding author upon reasonable request.

**Keywords:** Nickel oxide · Oxygen evolution reaction · Mxene · Ti3C2Tx

[1] E. Hu, Y. Feng, J. Nai, D. Zhao, Y. Hu, X. W. Lou, *Energy Environ. Sci.* **2018**, *11*, 872–880.
[2] F. Yu, H. Zhou, Y. Huang, J. Sun, *Nat. Commun.* **2018**, *9*, 2551.
[3] Y. Gong, Z. Yang, Y. Zhi, Y. Lin, T. Zhou, J. Li, F. Jiao, W. Wang, *Dalton Trans.* **2019**, *48*, 6718–6729.
[4] A. Raveendran, M. Chandran, R. Dhanusuraman, *RSC Adv.* **2023**, *13*, 3843–3876.
[5] Y. Zheng, Y. Jiao, A. Vasileff, S.-Z. Qiao, *Angew. Chem. Int. Ed.* **2018**, *57*, 7568–7579.
[6] T. Reier, H. N. Nong, D. Teschner, R. Schlögl, P. Strasser, *Adv. Energy Mater.* **2017**, *7*, 1601275.
[7] A. Ali, F. Long, P. K. Shen, *Electrochem. Energy Rev.* **2022**, *5*, 1.
[8] E. Fabbri, T. J. Schmidt, *ACS Catal.* **2018**, *8*, 9765–9774.
[9] G. Wu, X. Zheng, P. Cui, H. Jiang, X. Wang, Y. Qu, W. Chen, Y. Lin, H. Li, X. Han, Y. Hu, P. Liu, Q. Zhang, J. Ge, Y. Yao, R. Sun, Y. Wu, L. Gu, X. Hong, Y. Li, *Nat. Commun.* **2019**, *10*, 4855.
[10] D. Zheng, L. Yu, W. Liu, X. Dai, X. Niu, W. Fu, W. Shi, F. Wu, X. Cao, *Cell Rep. Phys. Sci.* **2021**, *2*.
[11] W. F. Chen, J. T. Muckerman, E. Fujita, *Chem. Commun.* **2013**, *49*, 8896–8909.
[12] R. Hutchings, K. Müller, R. Kötz, S. Stucki, *J. Mater. Sci.* **1984**, *19*, 3987–3994.
[13] Y. Lee, J. Suntivich, K. J. May, E. E. Perry, Y. Shao-Horn, *J. Phys. Chem. Lett.* **2012**, *3*, 399–404.
[14] J. Z. Y. Seow, T. D. Nguyen, *Electrochim. Acta* **2020**, *341*, 136058.
[15] M. Yu, E. Budiyanto, H. Tüysüz, *Angew. Chem. Int. Ed.* **2022**, *61*, e202103824.
[16] S. Geiger, O. Kasian, B. R. Shrestha, A. M. Mingers, K. J. J. Mayrhofer, S. Cherevko, *J. Electrochem. Soc.* **2016**, *163*, F3132.
[17] T. Noor, L. Yaqoob, N. Iqbal, *ChemElectroChem* **2021**, *8*, 447–483.
[18] I. Godwin, M. E. G. Lyons, *Electrochem. Commun.* **2013**, *32*, 39–42.

[19] D. S. Hall, D. J. Lockwood, C. Bock, B. R. MacDougall, *Proc. R. Soc. A* **2015**, *471*, 20140792.
[20] T. Jiang, T. Liu, S. Liu, Y. Wang, S. Gao, G. Montavon, S.-A. Ansar, H. Liao, *Appl. Mater. Today* **2022**, *28*, 101526.
[21] T. Jiang, X. Jiang, V. Kyriakou, K. Bouzek, H. Liao, *J. Mater. Chem. A* **2023**, *11*, 26011–26022.
[22] E. Fabbri, M. Nachtegaal, T. Binninger, X. Cheng, B.-J. Kim, J. Durst, F. Bozza, T. Graule, R. Schäublin, L. Wiles, M. Pertoso, N. Danilovic, K. E. Ayers, T. J. Schmidt, *Nat. Mater.* **2017**, *16*, 925–931.
[23] X. Liu, K. Ni, B. Wen, R. Guo, C. Niu, J. Meng, Q. Li, P. Wu, Y. Zhu, X. Wu, L. Mai, *ACS Energy Lett.* **2019**, *4*, 2585–2592.
[24] N. Hales, T. J. Schmidt, E. Fabbri, *Curr. Opin. Electrochem.* **2023**, *38*, 101231.
[25] W. Wu, Y. Wu, D. Zheng, K. Wang, Z. Tang, *Electrochim. Acta* **2019**, *320*, 134568.
[26] M. You, X. Du, X. Hou, Z. Wang, Y. Zhou, H. Ji, L. Zhang, Z. Zhang, S. Yi, D. Chen, *Appl. Catal., B* **2022**, *317*, 121729.
[27] D. Tyndall, L. Gannon, L. Hughes, J. Carolan, S. Pinilla, S. Jaśkaniec, D. Spurling, O. Ronan, C. McGuinness, N. McEvoy, V. Nicolosi, M. P. Browne, *npj 2D Mater. Appl.* **2023**, *7*, 15.
[28] J. Liu, C. Wang, F. Rong, S. Wu, K. Tian, M. Wang, L. He, Z. Zhang, M. Du, *Electrochim. Acta* **2020**, *334*, 135653.
[29] L. Yan, J. Liang, D. Song, X. Li, H. Li, *Adv. Funct. Mater.* **2024**, *34*, 2308345.
[30] L. Yan, Y. Chen, J. Xie, H. Li, *Small* **2024**, *20*, 2403596.
[31] M. Naguib, M. Kurtoglu, V. Presser, J. Lu, J. Niu, M. Heon, L. Hultman, Y. Gogotsi, M. W. Barsoum, *Adv. Mater.* **2011**, *23*, 4248–4253.
[32] B. Anasori, M. R. Lukatskaya, Y. Gogotsi, *MXenes*, Jenny Stanford Publishing, **2023**, 677–722.
[33] W. Hong, B. C. Wyatt, S. K. Nemani, B. Anasori, *MRS Bull.* **2020**, *45*, 850–861.
[34] M. Naguib, M. W. Barsoum, Y. Gogotsi, *Adv. Mater.* **2021**, *33*, 2103393.
[35] C. Kaplan, R. M. Restrepo, T. Schultz, K. Li, V. Nicolosi, N. Koch, M. P. Browne, *Electrochim. Acta* **2024**, *490*, 144269.
[36] J. L. Hart, K. Hantanasirisakul, A. C. Lang, B. Anasori, D. Pinto, Y. Pivak, J. T. van Omme, S. J. May, Y. Gogotsi, M. L. Taheri, *Nat. Commun.* **2019**, *10*, 522.
[37] M. Naguib, M. W. Barsoum, Y. Gogotsi, *Adv. Mater.* **2021**, *33*, 1–10.
[38] F. Shahzad, M. Alhabeb, C. B. Hatter, B. Anasori, S. M. Hong, C. M. Koo, Y. Gogotsi, *Science* **2016**, *353*, 1137–1140.
[39] W. Sun, S. A. Shah, Y. Chen, Z. Tan, H. Gao, T. Habib, M. Radovic, M. J. Green, *J. Mater. Chem. A* **2017**, *5*, 21663–21668.
[40] a) M. Yu, S. Zhou, Z. Wang, J. Zhao, J. Qiu, *Nano Energy* **2018**, *44*, 181–190; b) C. Hao, Y. Wu, Y. An, B. Cui, J. Lin, X. Li, D. Wang, M. Jiang, Z. Cheng, S. Hu, *Mater. Today Energy* **2019**, *12*, 453–462; c) H. Huang, B. Shen, M. Yan, H. He, L. Yang, Q. Jiang, G. Ying, *Fuel* **2022**, *328*, 125234.
[41] Y. Lu, D. Fan, Z. Chen, W. Xiao, C. Cao, X. Yang, *Sci. Bull.* **2020**, *65*, 460–466.
[42] H. Jia, P. Guan, Y. Zhou, Z. Feng, R. Zhu, M. Li, T. Wan, T. Huang, T. Liang, J. Pan, Z. Ma, Y. Xu, C. Wang, D. Chu, *Energy Fuels* **2022**, *36*, 13808–13816.
[43] A. Vazhayil, L. Vazhayal, S. Ashok, C. J. Thomas, N. Thomas, *ChemCatChem* **2024**, *16*, e202301250.
[44] B. Zhang, Z. Du, R. Sun, X. Lai, J. Lan, X. Liu, L. Yan, *ACS Appl. Mater. Interfaces* **2022**, *14*, 47529–47541.
[45] L. Yan, Z. Du, X. Lai, J. Lan, X. Liu, J. Liao, Y. Feng, H. Li, *Int. J. Hydrog. Energy* **2023**, *48*, 1892–1903.
[46] N. Fairley, V. Fernandez, M. Richard-Plouet, C. Guillot-Deudon, J. Walton, E. Smith, D. Flahaut, M. Greiner, M. Biesinger, S. Tougaard, D. Morgan, J. Baltrusaitis, *Appl. Surf. Sci. Adv.* **2021**, *5*, 100112.
[47] C. C. L. McCrory, S. Jung, J. C. Peters, T. F. Jaramillo, *J. Am. Chem. Soc.* **2013**, *135*, 16977–16987.
[48] D. Wang, B. Guan, Y. Li, D. Li, Z. Xu, Y. Hu, Y. Wang, H. Zhang, *J. Alloys Compd.* **2018**, *737*, 238–247.
[49] E. P. Alsaç, K. Zhou, W. Rong, S. Salamon, J. Landers, H. Wende, R. D. L. Smith, *Energy Environ. Sci.* **2022**, *15*, 2638–2652.
[50] Y. Wen, T. E. Rufford, X. Chen, N. Li, M. Lyu, L. Dai, L. Wang, *Nano Energy* **2017**, *38*, 368–376.
[51] M. C. Biesinger, L. W. M. Lau, A. R. Gerson, R. S. C. Smart, *Phys. Chem. Chem. Phys.* **2012**, *14*, 2434–2442.
[52] V. Natu, M. Benchakar, C. Canaff, A. Habrioux, S. Célérier, M. W. Barsoum, *Matter* **2021**, *4*, 1224–1251.
[53] M. Buldu-Akturk, T. Schultz, N. Sharma, U. Michalczik, P. Bogdanoff, N. Koch, M. P. Browne, *Electrochimica Acta* **2025**, *513*, 145529.
[54] R. L. Doyle, I. J. Godwin, M. P. Brandon, M. E. G. Lyons, *Phys. Chem. Chem. Phys.* **2013**, *15*, 13737–13783.
[55] H. Radinger, P. Connor, S. Tengeler, R. W. Stark, W. Jaegermann, B. Kaiser, *Chem. Mater.* **2021**, *33*, 8259–8266.
[56] M. W. Louie, A. T. Bell, *J. Am. Chem. Soc.* **2013**, *135*, 12329–12337.
[57] N. A. Saguì, P. Ström, T. Edvinsson, İ. Bayrak Pehlivan, *ACS Catal.* **2022**, *12*, 6506–6516.
[58] W. Lv, J. Zhu, F. Wang, Y. Fang, *J. Mater. Sci. - Mater. Electron.* **2018**, *29*, 4881–4887.
[59] D. B. Lioi, G. Neher, J. E. Heckler, T. Back, F. Mehmood, D. Nepal, R. Pachter, R. Vaia, W. J. Kennedy, *Acs Appl. Nano Mater.* **2019**, *2*, 6087–6091.
[60] X. Y. Liu, L. Wang, S. Ji, V. Linkov, Q. Q. Fu, Z. C. Li, H. Wang, *Dalton T.* **2023**, *52*, 9721–9730.
[61] H. Dau, C. Limberg, T. Reier, M. Risch, S. Roggan, P. Strasser, *ChemCatChem* **2010**, *2*, 724–761.
[62] W. Y. Chen, S. N. Lai, C. C. Yen, X. F. Jiang, D. Peroulis, L. A. Stanciu, *ACS Nano* **2020**, *14*, 11490–11501.
[63] O. Diaz-Morales, D. Ferrus-Suspedra, M. T. M. Koper, *Chem. Sci.* **2016**, *7*, 2639–2645.
[64] P. P. Tan, R. W. Gao, Y. W. Zhang, N. Han, Y. Z. Jiang, M. W. Xu, S. J. Bao, X. Zhang, *J. Colloid Interface Sci.* **2023**, *630*, 363–371.

Manuscript received: November 29, 2024
Revised manuscript received: January 31, 2025
Version of record online: February 28, 2025